Chinese Chemical Letters 32 (2021) 2027–2032

Contents lists available at ScienceDirect

Chinese Chemical Letters

journal homepage: www.elsevier.com/locate/cclet

Communication

One-pot synthesis of CoO–ZnO/rGO supported on Ni foam for high-performance hybrid supercapacitor with greatly enhanced cycling stability

Mingsheng Xu[a,1], Mingze Sun[a,1], Sajid ur Rehman[a], Kangkang Ge[a], Xiaolong Hu[a], Haizhen Ding[a], Jichang Liu[b], Hong Bi[a,*]

[a] School of Chemistry and Chemical Engineering, Anhui University, Hefei 230601, China
[b] State Key Laboratory of Chemical Engineering, East China University of Science and Technology, Shanghai 200237, China

ARTICLE INFO

Article history:
Received 6 November 2020
Received in revised form 6 December 2020
Accepted 7 December 2020
Available online 11 December 2020

Keywords:
Supercapacitor
Metal oxide
Graphene oxide
Energy density
Cycling stability

ABSTRACT

The high specific capacitance along with good cycling stability are crucial for practical applications of supercapacitors, which always demands high-performance and stable electrode materials. In this work, we report a series of ternary composites of CoO-ZnO with different fractions of reduced graphene oxide (rGO) synthesized by in-situ growth on nickel foam, named as CZG-1, 2 and 3, respectively. This sort of binder-free electrodes presents excellent electrochemical properties as well as large capacitance due to their low electrical resistance and high oxygen vacancies. Particularly, the sample of CZG-2 (CoO-ZnO/rGO 20 mg) in a nanoreticular structure shows the best electrochemical performance with a maximum specific capacitance of 1951.8 F/g (216.9 mAh/g) at a current intensity of 1 A/g. The CZG-2-based hybrid supercapacitor delivers a high energy density up to 45.9 Wh/kg at a high power density of 800 W/kg, and kept the capacitance retention of 90.1% over 5000 charge-discharge cycles.

Nowadays, emerging wearable and smart electronics call for the development of efficient and high-performance energy storage and conversion devices [1]. Supercapacitors (SCs) with superior capacitance, ultrahigh power density and excellent cyclic stability greatly satisfy the requirements of fast-charging, safety and stability in consumer markets, which have aroused more and more research interests in the past decades [2–4]. Traditional SCs store charges *via* electrostatic interaction at the electrode-electrolyte interface, this kind of charge storage mechanism usually described as electric double-layer capacitance (EDLC). Carbon materials (*e.g.*, activated carbon, carbon nanotube and graphene with unique large specific surface area) mediated by an EDLC charge storage behavior possess higher charging rates as well as more stable cyclic stabilities when compared to pseudocapacitive electrode materials [2,5,6]. As each coin has two sides, the EDLC occurs purely at the surface of electrode and thus greatly limits the quantity of absorbed charges, while pseudocapacitive electrode materials could store a large amount of charges by interfacial fast faradic reactions. Therefore, it leaves plenty of room for developing hybrid SCs that combine the superiority of single EDLC-type and pseudocapacitive electrode materials, in the meanwhile, to realize ultrahigh capacity without compromising the excellent power ability, rate ability and cyclic stability [7–10].

Nanoscaled transition metal oxides (*e.g.*, CoO and ZnO), have been considered as promising pseudocapacitive electrode materials owing to their high theoretical specific capacitance, easy availability, low cost and great chemical stability [11–14]. Among various metal oxide materials, ZnO has attracted much attention as an efficient electrode material when used in energy storage device with good electrochemical activity, environmental friendliness, low cost and easy manufacturing [15,16]. However, the low electron transportation efficiency and intrinsic resistance result in the actual capacity being much lower than the theoretical value, which restricts their application in high energy density pseudocapacitors [17]. Moreover, the formation and breakage of chemical bonds accompanied with the serious volume change and structural destruction during faradic electron transfer process greatly decreases the long-term cyclic stability of such transition metal oxides as electrode materials [18]. In general, the improvement of electron transfer efficiency has realized by using nanosized materials because of their higher specific surface area and thus more exposure of electrochemical active sites to electrolyte. Therefore, hybrid nanostructured electrodes are preferred, for

* Corresponding author.
E-mail address: bihong@ahu.edu.cn (H. Bi).
[1] These authors contributed equally to this work.

https://doi.org/10.1016/j.cclet.2020.12.011

example, nanostructured metal oxides/carbon or metal oxides/conducting polymers, as they can synergistically improve the intrinsic electron-transfer rate, electrochemical reactivity and cyclic stability [19–21].

Up to date, various conducting carbon materials, such as carbon nanotubes, carbon nanofilms, carbon nanofibers, carbon paper, carbon microspheres, graphene or reduced graphene oxide (rGO) have been applied as the matrix for anchoring the transition metal compound [7,22–24]. More recently, Huang *et al*. used microwave radiation to accelerate the hydrothermal growth rate of nanostructured $ZnCo_2O_4$/ZnO/carbon nanotubes, leading to a higher capacity and a better cycling stability [25]. Kumar *et al*. reported the enhanced electrochemical performance of the mesoporous $NiFe_2O_4$ and multiwalled carbon nanotubes nanocomposites synthesized by a hexamethylene tetramine-assisted one-pot hydrothermal approach [26]. Hou *et al*. developed a two-step solvothermal methodology to efficiently prepare monodispersed H-$NiCoSe_2$ sub-microspheres as electroactive material for high-performance electrochemical supercapacitors. The formation process and intrinsic charge-storage mechanism of such pseudocapacitive material were also revealed [27].

Despite this progress, the specific capacitance of transition metal oxides remains far below the theoretical value, accompanied with moderate power density and rate performance. Besides, the complexity of the current synthesis routes and preparation procedures of electrode materials hinders their application for scaling up. Meanwhile, the relationship between structure and performance needs to be further investigated, for instance, the influence of oxygen vacancy on the enhancement of capacitive energy storage of the CoO-ZnO electrode materials. Therefore, it is still urgent to develop advanced electrode nanomaterials for high-performance SCs as well as clearly understood charge storage mechanism.

Here, we report a series of CoO-ZnO/rGO@Ni foam (CZG) nanocomposites synthesized by one-pot hydrothermal method and subsequent annealing treatment, showing high performance as electrode materials in SCs. Since both CoO and ZnO are pseudocapacitive electrode materials and the hybrid CoO-ZnO compound should have a greater capacitance. Besides, as an excellent charge storage 2D planer matrix with a high specific surface area and a good electron transfer capability, rGO is expected to provide more space for anchoring the high-performance nanostructured metal oxides. This hybrid electrode structure can make more active sites of metal oxides exposed to electrolyte and thus increase the contact area between electrolyte ions and CoO-ZnO electrode surface to achieve their high theoretical capacitance. As previously reported, the introduction of conductive rGO into a three-dimensional metal oxides nanostructure along with abundant oxygen vacancies (O-) on the surface of metal oxides can greatly enhance the electron-transfer efficiency as well as charge-discharge cycle stability of the electrodes [28–32]. In addition, the hybrid SCs fabricated by metal oxides-based positive electrode and porous graphene hydrogel electrode (PGH, negative electrode) can broaden a potential window in aqueous electrolyte and present a high energy density at a high power density simultaneously [31–33]. Therefore, in the present work, CZG//PGH hybrid SC is designed and fabricated to show a high supercapacitance as well as an excellent charge-discharge cycle stability.

Firstly, preparation of binder-free electrode based on CoO-ZnO (CZ)@Ni foam. The Ni foam was cut into a size of 1 cm × 1 cm, and then ultrasonically cleaned with acetone, 3 mol/L HCl, deionized water and ethanol for 15 min to remove surface impurities and oxide layers. Then, the washed Ni foam was kept at 50 °C in an oven and dried for 6 h [31]. CZ@Ni foam was synthesized, in the meanwhile, the binder-free electrode based on CZ@Ni foam was prepared according to the previous work [32]. Briefly, Zn $(CH_3COO)_2{\cdot}2H_2O$ (0.5 mmol), $Co(NO_3)_2{\cdot}6H_2O$ (0.5 mmol), NH_4F (3.0 mmol) and $CO(NH_2)_2$ (6.0 mmol) were dispersed in 30 mL of deionized water. The liquid was then transferred to a Teflon-lined stainless-steel autoclave (50 mL) and the washed Ni foam was immersed into the solution. Subsequently, the autoclave was heated to 120 °C and then kept for 6 h in an oven. When the reaction was finished, the autoclave was cooled to room temperature naturally and the CZ sample grown in-situ on the Ni foam was washed with deionized water and dried at 50 °C for 6 h. Finally, the sample was placed in a tube furnace, heated to 400 °C under a nitrogen atmosphere with a heating rate 5 °C/min, and then kept heating at 400 °C for 2 h to yield the CZ@Ni foam-based electrode.

Secondly, preparation of binder-free electrode based on CoO-ZnO/rGO (CZG)@Ni foam. GO was firstly prepared from graphite powder by an improved Hummer method [34–36]. Briefly, 0.5 g of graphite powder was mixed with 20 mL of H_2SO_4 (98 wt%) in a conical flask and stirred for 30 min in an ice bath. Then, 0.5 g of $NaNO_3$ and 3.0 g of $KMnO_4$ were added slowly into the solution under continuous stirring and then stirred for two more hrs. After that, the solution was diluted with 40 mL of deionized water, and then10 mL of H_2O_2 (30 wt%) and 100 mL of deionized water were added in turn to the above solution. Finally, the brownish yellow GO powder was obtained after filtration, washing (with 0.5 mol/L HCl solution and deionized water) and lyophilization. The CoO-ZnO/rGO (CZG)@Ni foam was synthesized and in the meantime the binder-free CZG@Ni foam-based electrode was prepared according to the same procedure of CZ@Ni foam-based electrode as above-mentioned, except adding different amount of GO (10 mg, 20 mg and 40 mg) into the Co and Zn-precursor solution respectively in the first step. Finally, the obtained CZG@Ni foam-based electrodes were defined as CZG-1 (10 mg), CZG-2 (20 mg) and CZG-3 (40 mg), respectively. The mass loading of the CZG on Ni foam was about 8 mg/cm^2.

Preparation of porous graphene hydrogel (PGH) electrode and fabrication of CZG//PGH hybrid supercapacitor (CZG//PGH HSC). To prepare porous graphene hydrogel electrode, 80 mg of GO was dissolved in 20 mL of deionized water and sonicated for 1 h to form a homogeneous suspension and then transferred into a 50 mL, Teflon-lined stainless steel autoclave. After heating at 180 °C for 12 h, the PGH was obtained and then pressed onto a nickel foam to be as a negative electrode. The mass loading of the PGH on Ni foam was about 8 mg/cm^2. On the other hand, the positive electrode was chosen from the afore-mentioned CZ@Ni foam-based electrode and a series of CZG@Ni foam-based electrodes (CZG-1, CZG-2 and CZG-3). Then, a new asymmetric supercapacitor (CZG//PGH) was fabricated when 3 mol/L KOH-soaked separator was sandwiched between the CZG positive electrode and PGH negative electrode. To obtain the optimum performance of the asymmetric supercapacitor, we should balance the charge of the two electrodes. First, we need to calculate the specific capacitance and the stored charges of either positive or negative electrode by integrating the CV curves with the following equations (Eqs. 1 and 2):

$$C = \frac{(\int IdV)}{\nu m \Delta V} \tag{1}$$

$$q = C \times \Delta V \times m \tag{2}$$

Where I, V, ν, m and ΔV are the current (A), potential (V), scan rate (mV/s), mass of the active electrode materials (g) and potential window (V) of the CV test, respectively. And C represents the specific capacitance of single electrode calculated by CV test at a

scan rate of 10 mV/s with a three-electrode configuration. Subsequently, we calculate the optimum mass ratio of positive (m_+) and negative (m_-) electrode *via* charge balance equation (Eq. 3):

$$\frac{m_+}{m_-} = \frac{C_- \times \Delta V_-}{C_+ \times \Delta V_+} \tag{3}$$

Morphology was observed by employing a scanning electron microscope (SEM, s-4800) and a transmission electron microscope (TEM, JEM-2100). Energy dispersive spectrometer (EDS) test was carried out on the s-4800. X-ray diffraction (XRD) was performed on the X'pert PRO diffractometer at a scanning rate of 20°/min, with the Cu-Kα radiation (λ =1.54056 Å). High-resolution transmission electron microscope (HR-TEM) images and the selected area electron diffraction (SAED) patterns were recorded on the JEM-2100. Besides, the samples were tested with an X-ray photoelectron spectroscopy (XPS, ESCALAB 250). Electron paramagnetic resonance (EPR) spectra were taken with a Bruker EMXnano system at 9.4 GHz X band and measured at 25 °C.

To evaluate the electrochemical performance of the CoO-ZnO/rGO compounds, a three-electrode electrochemical cell was fabricated when CZG@Ni foam, platinum plate and saturated calomel electrode (SCE) were used as working electrode, counter electrode and reference electrode, respectively. The potential window of cyclic voltammetry (CV) test was ranging from -0.2 V to 0.4 V with scan rates changing from 10 mV/s to 100 mV/s. Besides, the operation potential of galvanostatic charge-discharge (GCD) curves were set from 0.0 V to 0.4 V with current densities ranging from 1.0 A/g to 10 A/g. Electrochemical impedance spectroscopy (EIS) measurement was performed to obtain impedance information of the as-prepared materials. The frequency of EIS test was ranging from 100 kHz to 10 mHz at open circuit conditions with an AC voltage amplitude of 5 mV.

The specific capacitance (C_m) (F/g) and capacity (mAh/g) in a three-electrode system are calculated from the GCD curves according to the following equation (Eq. 4) [37].

$$C_m = \frac{It}{m\Delta V}\left(Capacity = \frac{C_m \times \Delta V}{3.6}\right) \tag{4}$$

Among them: constant current I (A), discharge time t (s), the mass of the active material m (g) and discharge voltage ΔV (V).

To evaluate the full performance in a full supercapacitor cell, CV and GCD measurements of CZG//PGH HSC were carried out in a two-electrode system. The specific capacitance C_{HSC} (F/g), energy density E (Wh/kg) and power density P (W/kg) of the device are calculated according to the GCD curve using the following Eqs. 5–7 [38]:

$$C_{HSC} = \frac{It}{m\Delta V} \tag{5}$$

$$E = \frac{C_{HSC}\Delta V^2}{2} \tag{6}$$

$$P = \frac{E}{t} \tag{7}$$

Where ΔV (V) is the potential window, I (A) is the current, m (g) is the sum of mass load of negative and positive electrodes, t (s) is the discharge time.

Fig. 1a shows a schematic synthesis process of CZG@Ni foam. The morphologies of the obtained CZ@Ni foam and CZG@Ni foam samples (CZG-1, CZG-2, CZG-3) were examined using SEM. Fig. 1b shows the SEM image of CZ@Ni foam, presenting a clustered

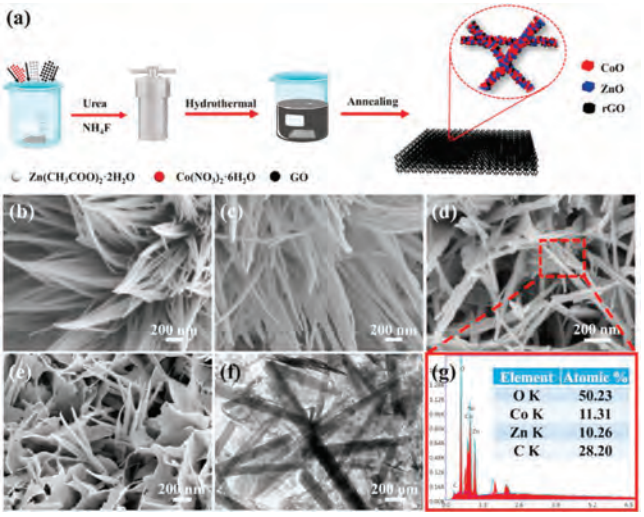

Fig. 1. (a) Schematic synthesis process of CZG@Ni foam. SEM images of the (b) CZ, (c) CZG-1, (d) CZG-2 and (e) CZG-3. (f) TEM image and (g) the EDS of the CZG-2 (Ni foam removed).

nanowires similar to chrysanthemums. After composite with rGO, the diameter of CZ nanowires increases systematically as shown in Figs. 1c-f, which is more beneficial for electron migration. Notably, the SEM image of CZG-2 (Fig. 1d) shows that rGO has self-assembled into pieces similar to the shape of chrysanthemum and the CZ nanowires linked together. The formation of such kind of structure could enhance the transmission path of electrons within the active layer of electrode. Fig. 1e shows the morphology of the obtained CZG-3 by increasing the rGO amount. The BET and BJH data (Table S1 in Supporting information) showed the specific surface area and pore volume of CZG samples get increased when increasing the content of rGO. Unfortunately, the excessive increase of rGO led to the continuous stacking of structures and the formation of nanoscaled sheets, which may prevent the electrolyte from fully contacting with the electrode material and then affect the ultimate electrochemical performance. Fig. 1f shows the TEM image of CZG-2 peeled from the Ni foam that still keeps the interwoven nanowires structure. Its corresponding EDS spectrum (Fig. 1g) indicates the presence of Co, Zn, O and C elements with atomic ratios of 11.31%, 10.26%, 50.23% and 28.20%, respectively, which confirms the formation of zinc oxide, cobalt oxide and r-GO in the sample of CZG-2.

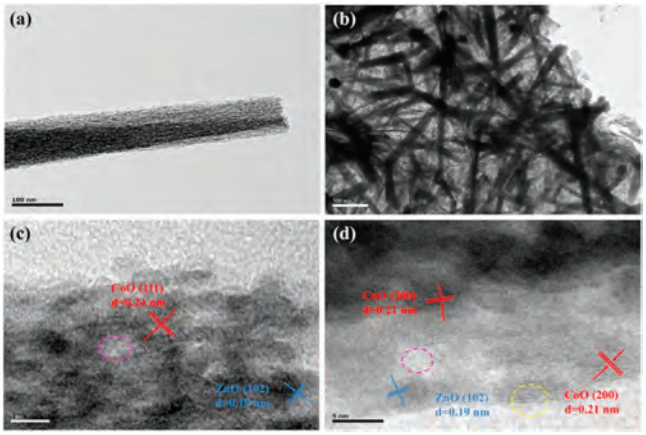

Fig. 2. TEM images of (a) CZ and (b) CZG-2 (Ni foam removed). (c,d) HR-TEM images of the CZG-2 as shown in (b).

For more comparison, Figs. 2a and b show typical TEM images of a single CZ nanowire and the CZG-2 peeled from the Ni foam, respectively. It is obvious that the interwoven nanowires entangled with rGO sheet in the sample of CZG-2, which is far different from that of CZ sample. Further, Figs. 2c and d display the corresponding HRTEM images of the CZG-2 sample as shown in Fig. 2b. Lattice fringes can be seen clearly in the HRTEM images, where the lattice spacing of 0.21 nm (200) and 0.24 nm (111) belongs to CoO (marked in red dotted circle), while the lattice spacing of 0.19 nm (102) belongs to ZnO (marked in blue dotted circle) [39,40]. Nanocrystalline ZnO and CoO have grown together closely to form CZ nanowires and entangled with rGO [40], as shown in Fig. 2b. However, the lattice fringes at the edges blurred due to defects on the surface [41]. Within the yellow dotted circle in Fig. 2d, there are obvious lattice defects at the edge, such as crystal dislocation and lattice distortion, which can increase the activity of the electrode material and improve its electrochemical performance [42]. The voids (marked in pink circle) may be caused by the lamination and interlacing between the ZnO and CoO nanocrystals. The ions in the electrolyte can penetrate through these voids to contact with the electrode active material more thoroughly, which enhances the charge storage ability of the electrode [43].

The XRD patterns of CZ, CZG-1, CZG-2 and CZG-3 are shown in Fig. S1 (Supporting information), where the diffraction peaks of both ZnO and CoO crystals can be seen clearly in these four samples. The diffraction peaks of ZnO hexagonal crystals (JCPDS No. 65-3411) locate at $2\theta = 31.77^\circ$, 34.42°, 36.26°, 47.54°, 56.60°, 62.86°, 66.38°, 67.95° and 69.09°, corresponding to (100), (002), (101), (102), (110), (103), (200), (112) and (201) crystal planes, respectively. As for the cubic CoO (JCPDS No. 65-2902), the diffraction peaks at $2\theta = 36.50^\circ$, 42.40°, 61.51°, 73.69° and 77.56° correspond to (111), (200), (220), (311) and (222) crystal planes, respectively [32]. Fig. S1 also shows the XRD of GO having a sharp peak at 24.9°. While for GO, after hydrothermal treatment, the peak has vanished and is replaced by a broad hump. This hump is visibly present in all the three samples of CZG-1, CZG-2 and CZG-3. In addition, the XPS data of CZ (Fig. S2 in Supporting information), CZG-1 (Fig. S3 in Supporting information), CZG-2 (Fig. S4 in Supporting information) and CZG-3 (Fig. S5 in Supporting information) reveal the chemical valence state of Zn and Co in these samples. As shown in Fig. S4b, the characteristic peaks at 1021.1 eV and 1044.2 eV can be attributed to the Zn 2p orbital in CZG-2 sample. In Fig. S4c, the XPS spectrum of Co 2p shows two characteristic peaks at 780.0 eV and 795.2 eV and two satellite peaks at 789.0 eV and 804.8 eV, demonstrating the co-existence of Co^{2+} (782.6 eV, 798.5 eV) and Co^{3+} (780.0 eV, 795.2 eV) in CZG-2 sample. This kind of mixed valence state confirms the pseudocapacitive behavior of the CZG composite material [43], because Co^{2+} can convert into Co^{3+} through electronic loss [44]. Such a Faradic redox reaction may lead to the improvement of electrochemical performance [45]. Fig. S4d shows the spectrum of C 1s, suggesting the main existence of C—C and also the presence of a certain amount of C—O and C=O bonds in the sample of CZG-2, these oxygen-containing groups are derived from the surface functional groups on the rGO [46].

To investigate the density of oxygen vacancies in the samples, EPR measurement was carried out. When the oxygen in the crystal becomes free oxygen, electrons are released and captured by the EPR to generate a signal [28,29]. Fig. S6 (Supporting information) shows the EPR spectra of four samples of CZ, CZG-1, CZG-2 and CZG-3, which have g values of 1.9840, 1.9837, 1.9828 and 1.9833, respectively. These g values are very close to the previously reported binary and ternary metal oxides such as NiO-CuO and CoO-NiO-ZnO, which indicates the presence the oxygen vacancy in metal oxides [32,43]. The strongest signal of CZG-2 suggests the highest oxygen vacancy density in this sample, compared to those in samples of CZ, CZG-1 and CZG-3, which is in good agreement with the XPS O1 s analysis result (Fig. S7 in Supporting information). As shown in Figs. S7a–d, these three peaks (O1, O2 and O3) can be identified clearly in samples of CZ, CZG-1, CZG-2 and CZG-3. Correspondingly, their peak area ratios of O2 to O1 (O2/O1) are 0.596, 0.482, 0.630 and 0.379, respectively. The largest O2/O1 ratio of the CZG-2 sample means the increased O-vacancies compared to samples of CZ, CZG-1 or CZG-3, which is probably related to a huge number of lattice defects with lower oxygen coordination in the CZG-2 sample.

The Raman spectroscopy was employed to investigate the structural defects of the CZG samples with different fractions of rGO. The D-band peak of the Raman spectrum in Fig. S8 (Supporting information) appears around 1360 cm^{-1} is due to

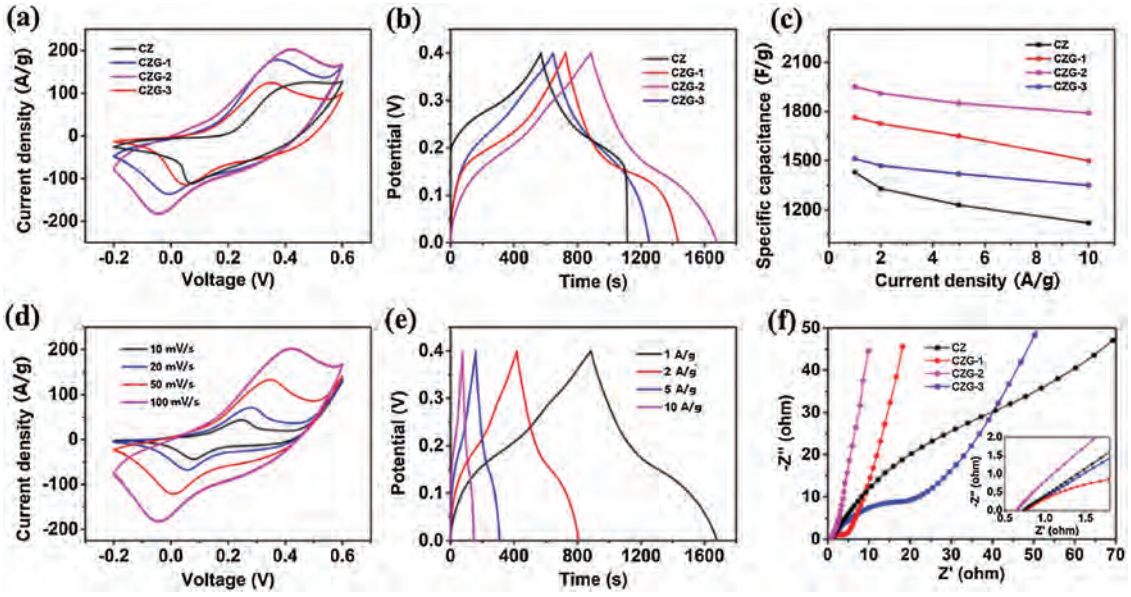

Fig. 3. (a) CV at scan rate of 100 mV/s and (b) GCD curves at the current density of 1 A/g of the electrodes with different samples. (c) The specific capacitance of CZ, CZG-1, CZG-2 and CZG-3 hybrid electrodes at different current densities. (d) CV curves at scan rate ranging from 10 mV/s to 100 mV/s. (e) GCD curves at the current density ranging from 1 A/g to 10 A/g of CZG-2. (f) Nyquist plots of CZ, CZG-1, CZG-2 and CZG-3 hybrid electrodes.

hybrid vibrations at the edge of the graphene, often referred to as a defect band or disordered band [47]. At the same time, the G-band peak appears around 1600 cm^{-1} indicates the stretching vibration of carbon atoms in graphene in the plane, known as an ordered band. The D peak area and G peak area of each sample were respectively integrated, and the I_D/I_G of CZ, CZG-1, CZG-2 and CZG-3 samples are 1.42, 1.40, 1.32 and 1.25, respectively, indicating that the electrochemical performance could be significantly improved with a proper amount of defects [48].

The cyclic voltammetry (CV) was performed at a scan rate of 100 mV/s to test the CZ, CZG-1, CZG-2 and CZG-3 samples, and results are shown in Fig. 3a. It can be clearly seen from the figure that regardless of the amount of rGO, all the four samples show a pair of obvious redox peaks, which indicates that they all possess obvious Faraday pseudocapacitance characteristics. In addition, the sample CZG-2 with the addition of 20 mg rGO has the largest area enclosed by the CV curve at the same scan rate, *i.e.*, the highest specific capacitance. From the GCD curves, the specific capacitance (capacity) of these four samples were calculated according to Eq. 4. Fig. 3b shows that the specific capacitance (capacity) of CZ, CZG-1, CZG-2 and CZG-3 at the current density of 1 A/g are 1429.2 F/g (158.8 mAh/g), 1763.4 F/g (195.9 mAh/g), 1951.8 F/g (216.9 mAh/g) and 1512.1 F/g (168.0 mAh/g), respectively. Among all, CZG-2 has the highest specific capacitance value at the same current density, which is due to its excellent 3D interwoven network structure and the highest oxygen vacancy density as above-mentioned. When further increase the content of rGO in CZG samples, the charging and discharging platform becomes more and more invisible, demonstrating a decrease of pseudocapacitance. This is because the excessive addition of rGO destroy the well-interlinked 3D interwoven structure of CZG electrode and form a compact flake. Therefore, the active sites of CZG are partially covered and thus decrease the pseudocapacitance of CZG.

Fig. 3c shows a good rate performance of CZ, CZG-1, CZG-2 and CZG-3 electrode materials. When the current density increases, the specific capacitance will decrease to a certain extent. CZG composite materials containing rGO have better rate performance compared with CZ that contains no rGO, which means that rGO can improve the electron transfer efficiency and electric conductivity of the electrode active layers. The capacitance retention of CZ, CZG-1, CZG-2 and CZG-3 are 78.2%, 85.1%, 91.7% and 89.3%, respectively. Among all, CZG-2 has the highest capacitance retention rate, *i.e.*, the best rate performance, which again emphasize the importance of constructing unique 3D interwoven structure of nanocomposite electrodes.

Fig. 3d shows the CV curves of CZG-2 sample at different scanning rates of 10, 20, 50 and 100 mV/s. As can be seen from the figure, with the increase of the scanning rate, the shape of the CV curve has no significant difference or change, which indicates that the CZG-2 has a better rate performance. When the scan rate is increased, the redox peaks "disappear", the reason may be that the ion movement was delayed due to the relaxation phenomenon, resulting in a Faraday redox reaction could not be detected promptly. On the other hand, the large scan rate also leads to a reduction in specific capacitance. Fig. 3e shows the charge-discharge test curves of CZG-2 samples at different current densities (1, 2, 5 and 10 A/g). The specific capacitance of CZG-2 was calculated *via* Eq. 4 and the values are 1951.8 F/g (1 A/g, 216.9 mAh/g), 1910.9 F/g (2 A/g, 212.3 mAh/g), 1850.2 F/g (5 A/g, 205.6 mAh/g) and 1790.3 F/g (10 A/g, 198.9 mAh/g) with a good rate capability of 91.7% retention.

To further test the performance of the electrode material, an EIS analysis was performed. This spectrum generally consists of a high frequency semi-arc (which may not be obvious) and a low frequency slightly curved line. The intercept of the left end of the semi-arc at high frequency and the intersection of the X-axis is the contact resistance (R_s) on the electrode, while the value of the semi-arc diameter represents the charge diffusion resistance (R_{ct}). As can be seen from the Fig. 3f, the R_s values of all the four samples are small and CZG-2 has the relatively smaller value among them, which is due to the introduction of appropriate amount of rGO and the in-situ growth on the nickel foam with good electrical conductivity. Besides, CZG-2 also has the minimum R_s and R_{ct} values, and the nearly vertical shape in the low-frequency region of Nyquist plots, indicating that it possesses the strongest capacitive characteristics.

Fig. 4a demonstrates the assembly process of CZG-2//PGH HSC. Meanwhile, the CV curves of CZG-2 and PGH electrode are shown in Fig. 4b in a three-electrode configuration at the scan rate of 10 mV/s. The rectangular shape of PGH and reversible redox peaks of CGZ-2 further demonstrate the ideal capacitive property of PGH (251.5 F/g at 1 A/g, Fig. S9 in Supporting information) and faradic behavior of CGZ-2 electrode. The potential window of PGH ranges from −1.0 V to 0 V, and that of CZG-2 ranges from −0.2 V to 0.6 V.

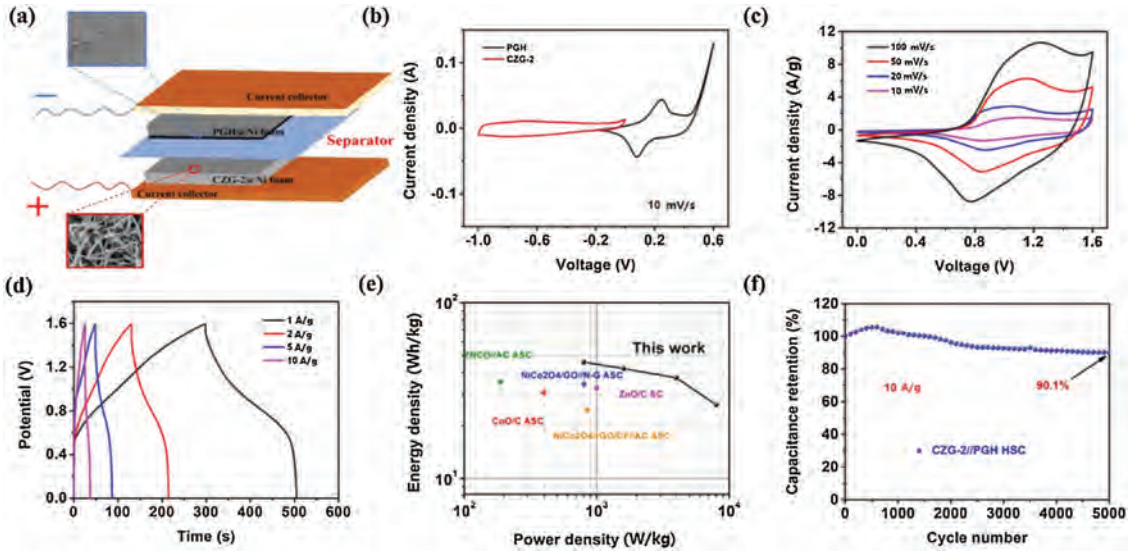

Fig. 4. (a) Schematic diagram of an hybrid supercapacitor. (b) Comparative CV curves of the CZG-2 positive electrode and the PGH negative electrode measured at a scan rate of 10 mV/s in the three-electrode system. (c) CV curves (10-100 mV/s). (d) GCD curves (1-10 A/g). (e) Ragone plots of the HSC devices. (f) Cycling performance of the CZG-2//PGH HSC device.

Here, a hybrid supercapacitor was fabricated by using PGH and CZG-2 as negative and positive electrode material for a higher potential window.

After assembled as a hybrid supercapacitor, its potential window can be expanded to 1.6 V. Due to the increase of specific capacitance, the energy density of CZG-2//PGH HSC is also increased greatly. As shown in Fig. 4c, CZG-2//PGH HSC has a pair of redox peaks, which shows that after the introduction of rGO, a typical EDLC material, the CZG-2 still exhibits pseudocapacitor characteristics. In addition, as the scanning rate increases, the CV curve of CZG-2//PGH HSC does not change significantly, which indicates that CZG-2//PGH HSC has an excellent stability and multiplying rate performance. In Fig. 4d, the GCD curve shows a symmetrical charge-discharge process similar to that of a double-layer capacitor, indicating that the CZG-2//PGH HSC has excellent rapid charge transfer and rapid charge-discharge capacity. The specific capacitance of CZG-2//PGH HSC is calculated (Eq. 5) to be 129.1 F/g (1 A/g), 118.7 F/g (2 A/g), 105.1 F/g (5 A/g) and 83.1 F/g (10 A/g). Further, the energy density and power density of CZG-2//PGH HSC can be obtained according to Eqs. 6 and 7. Fig. 4e shows the Ragone plots of this work compared to the previously reported values, such as CoO/C ASC (30.9 Wh/kg at 398 W/kg) [11], $NiCo_2O_4$/GO//N-G ASC (34.4 Wh/kg at 800.0 W/kg) [19], ZnO/C SC (32.78 Wh/kg at 1000.0 W/kg) [21], $NiCo_2O_4$/rGO/CF//AC ASC (24.6 Wh/kg at 850.0 W/kg) [23] and ZNCO//AC ASC (35.6 Wh/kg at 187.6 W/kg) [49]. Obviously, the CZG-2//PGH HSC owns a high energy density of 45.9 Wh/kg (800 W/kg) and 26.3 Wh/kg (8 kW/kg). In Fig. 4f, in order to evaluate the cycle stability of CZG-2//PGH HSC, the 5000 charge-discharge cycles were tested at the current density of 10 A/g, it is notable that the retention of specific capacitance still remains 90.1%. Here, the capacitance increase of the initial hundreds of cycles is likely related to a cycling-induced "activation process" for Faradic pseudocapacitance of the CZG electrode [50–52]. Nevertheless, the capacitance retention kept above 90%, which is superior to most previously reported metal oxide electrodes [53,54]. The good cyclic stability demonstrates that the introduction of rGO in the CZG-2 sample as well as the interwoven nanostructure may help buffer the volume change and relax strain stress during charge-discharge process.

In summary, we have synthesized a novel series of CZG samples with different rGO fractions for high-performance supercapacitance. The CZG nanowires entangled with rGO sheet have grown in-situ on nickel foam by a simple hydrothermal method. Comparing with the other samples, the CZG-2 (containing rGO 20 mg) exhibits excellent electrochemical performance with a higher specific capacitance of 1951.8 F/g (216.9 mAh/g) at a current density of 1 A/g and a good rate capability (91.7% capacitance retention at 10 A/g). The superior capacitance behavior of CZG-2 can be attributed to its interwoven nanoreticular structure, an appropriate rGO content and the high oxygen vacancy density. Further, the CZG@Ni foam was used directly as a binder-free positive electrode and assembled with the PGH as a negative electrode to construct a hybrid supercapacitor. The CZG-2//PGH HSC delivers a high energy density of up to 45.9 Wh/kg at 800 W/kg with a decent cycling stability (90.1% capacitance retention after 5000 charge/discharge cycles). This work provides a successful example of using pseudocapacitive materials (for example, metal oxide nanomaterials) combined with EDLC materials like rGO to construct a high-performance hybrid supercapacitor in a binder-free mode for commercial application.

Declaration of competing interest

The authors declare that they have no known competing financial interests or personal relationships that could have appeared to influence the work reported in this paper.

Acknowledgments

The authors are thankful to the National Natural Science Foundations of China (No. 51772001). All of the authors also acknowledge the Key Laboratory of Environment-Friendly Polymer Materials of Anhui Province, Anhui University.

Appendix A. Supplementary data

Supplementary material related to this article can be found, in the online version, at doi:https://doi.org/10.1016/j.cclet.2020.12.011.

References

[1] S. Chu, A. Majumdar, Nature 488 (2012) 294–303.
[2] W. Fu, W. Han, H. Zha, et al., Phys. Chem. Chem. Phys. 18 (2016) 24471–24476.
[3] Y.Q. Jiang, J.P. Liu, Energy. Environ. Mater. 2 (2019) 30–37.
[4] W.Y. Liu, L.P. Li, Q.Y. Gui, et al., Acta Phys. Chim. Sin. 36 (2020) 1904049.
[5] S.H. Noh, W. Na, J.T. Jang, et al., Nano Lett. 12 (2012) 3716–3721.
[6] J. Balamurugan, T. Tran Duy, N.H. Kim, et al., J. Mater. Chem. A 4 (2016) 9555–9565.
[7] M. Zhou, B. Yang, Y. Zhao, et al., Cellulose 27 (2020) 1591–1601.
[8] C. Chen, G. Xu, X. Wei, et al., J. Mater. Chem. A 4 (2016) 9900–9909.
[9] Y. Ma, H. Chang, M. Zhang, et al., Adv. Mater. 27 (2015) 5296–5308.
[10] M.X. Chen, Y. Yang, D.Z. Chen, et al., Chin. Chem. Lett. 29 (2018) 564–570.
[11] N. Zhang, X.H. Yan, J. Li, et al., Electrochim. Acta 226 (2017) 132–139.
[12] H. Wang, C. Qing, J.T. Guo, et al., J. Mater. Chem. A 2 (2014) 11776–11783.
[13] Y. Xiao, A. Dai, X. Zhao, et al., J. Alloys Compd. 781 (2019) 1006–1012.
[14] M. Gao, W.K. Wang, Q. Rong, et al., ACS Appl. Mater. Inter. 10 (2018) 23163–23173.
[15] Y. Haldorai, W. Voit, J.J. Shim, Electrochim. Acta 120 (2014) 65–72.
[16] C.H. Kim, B.H. Kim, J. Power Sources 274 (2015) 512–520.
[17] A. Gonzalez, E. Goikolea, J. Andoni Barrena, et al., Renew. Sust. Energy Rev. 58 (2016) 1189–1206.
[18] I.H. Lo, J.Y. Wang, K.Y. Huang, et al., J. Power Sources 308 (2016) 29–36.
[19] J.W. Mao, C.H. He, J.Q. Qi, et al., J. Electron. Mater. 47 (2017) 512–520.
[20] C.W. Peng, J. Yu, S.H. Chen, et al., Chin. Chem. Lett. 30 (2019) 1137–1140.
[21] C. Sasirekha, S. Arumugam, G. Muralidharan, Appl. Surf. Sci. 449 (2018) 521–527.
[22] J. Qi, J. Mao, A. Zhang, et al., J. Mater. Sci. 53 (2018) 16074–16085.
[23] H. Jiang, K. Yang, P. Ye, et al., RSC Adv. 8 (2018) 37550–37556.
[24] Y. Liu, Z. Sun, X. Sun, et al., Angew. Chem. Int. Ed. 59 (2020) 2473.
[25] P. Huang, M. Zhang, J. Kang, et al., J. Mater. Sci. 54 (2019) 4154–4167.
[26] N. Kumar, A. Kumar, G.M. Huang, et al., Appl. Surf. Sci. 433 (2018) 1100–1112.
[27] L.R. Hou, Y.Y. Shi, C. Wu, et al., Adv. Funct. Mater. 28 (2018) 1705921.
[28] Y. Wang, T. Zhou, K. Jiang, et al., Adv. Energy Mater. 4 (2014) 1400696.
[29] T. Zhang, M.Y. Wu, D.Y. Yan, et al., Nano Energy 43 (2018) 103–109.
[30] Z. Luo, R. Miao, T.D. Huan, et al., Adv. Energy Mater. 6 (2016) 1600528.
[31] X. Zhang, J. Wang, J. Liu, et al., Carbon 115 (2017) 134–146.
[32] M. Sun, J. Wang, M. Xu, et al., Adv. Electro. Mater. 5 (2019) 1900397.
[33] J.F. Sun, C. Wu, X.F. Sun, et al., J. Mater. Chem. A. 5 (2017) 9443.
[34] W.S. Hummers, R.E. Offeman, J. Am. Chem. Soc. 80 (1958) 1339.
[35] X.Y. Zhai, P. Zhang, C.J. Liu, et al., Chem. Commun. 48 (2012) 7955–7957.
[36] L.J. Cote, F. Kim, J. Huang, J. Am. Chem. Soc. 131 (2009) 1043–1049.
[37] J. Ma, D.Y. Su, Z.G. Liu, et al., 3rd International Workshop on Renewable Energy and Development, 2019.
[38] J. Liu, S.U. Rehman, J. Wang, et al., Synth. Met. 246 (2018) 23–30.
[39] M. Wang, J. Ma, Q. Chang, et al., Ceram. Int. 44 (2018) 5250–5256.
[40] J.H. Choi, Y. Kim, B.S. Kim, J. Power Sources 454 (2020)227917.
[41] Y. Dong, Z.S. Wu, W. Ren, et al., Sci. Bull. 62 (2017) 724–740.
[42] H. Tan, Z. Zhao, W.B. Zhu, et al., ACS Appl. Mater. Inter. 6 (2014) 19184–19190.
[43] Z. Fang, Su. Rehman, M. Sun, et al., J. Mater. Chem. A 6 (2018) 21131–21142.
[44] R.M. Obodo, A.C. Nwanya, M. Arshad, et al., Int. J. Energy Res. 44 (2020) 3192–3202.
[45] Z. Zhang, X. Huang, H. Li, et al., J. Energy Chem. 26 (2017) 1260–1266.
[46] Y. Gong, D. Li, Q. Fu, et al., Prog. Nat. Sci-Mater. 25 (2015) 379–385.
[47] B. Zhao, J. Song, P. Liu, et al., J. Mater. Chem. 21 (2011) 18792–18798.
[48] J. Zhu, A.S. Childress, M. Karakaya, et al., Adv. Mater. 28 (2016) 7185–7192.
[49] C. Wu, J.J. Cai, Q.B. Zhang, et al., ACS Appl. Mater. Inter. 7 (2015) 26512–26521.
[50] C. Zhou, Y. Zhang, Y. Li, et al., Nano Lett. 13 (2013) 2078–2085.
[51] R. Li, Z. Lin, X. Ba, et al., Nanoscale Horiz. 1 (2016) 150–155.
[52] R.B. Rakhi, W. Chen, D. Cha, et al., Nano Lett. 12 (2012) 2559–2567.
[53] Y. Luo, H. Zhang, D. Guo, et al., Electrochim. Acta 132 (2014) 332–337.
[54] N. Liu, J. Li, W. Ma, et al., ACS Appl. Mater. Inter. 6 (2014) 13627–13634.